Received May 30, 2013, accepted August 19, 2013, date of publication August 22, 2013, date of current version August 30, 2013.

Digital Object Identifier 10.1109/ACCESS.2013.2279356

Effective Permittivity of 3-D Periodic Composites With Regular and Irregular Inclusions

AUSTIN J. PICKLES AND MICHAEL B. STEER (Fellow, IEEE)
Department of Electrical and Computer Engineering, North Carolina State University, Raleigh, NC 27695, USA

Corresponding author: A. J. Pickles (ajpickle@ncsu.edu)

This work was supported by the U.S. Office of Naval Research as a Multi-Disciplinary University Research Initiative on Sound and Electromagnetic Interacting Waves under Grant N00014-10-1-0958.

ABSTRACT This paper explores the effective temporal surface-illuminated properties of two-component composites consisting of inclusions of regularly- and irregularly-shaped crystals in a matrix. Time-domain electromagnetic modeling using the finite integration technique is used to calculate scattering (*S*-) parameters, and from these, the effective relative permittivities are calculated. It is shown that the orientation of inclusions with high permittivity contrast affects the effective electrical permittivity of a composite mixture. For both low and high contrast inclusions, fields localize at edges and corners of the irregular inclusion in a manner not dependent on boundary conditions used in simulation.

INDEX TERMS Cross-sectional area, effective permittivity, electric field, electromagnetic analysis, energetic materials, energy density, finite integration technique, HMX, irregular crystals, localization, mixing rules, relative permittivity, rotation.

I. INTRODUCTION

The detection and neutralization of energetic materials using stand-off techniques is of significant and growing importance [1]–[5]. Most solid energetic materials are random mixtures comprising irregularly-shaped explosive crystals embedded in a passive composite or binder. In part, the energetic material can be characterized by its steady-state bulk electrical permittivity. However, with standoff electromagnetic (EM) probing, the probe will interact with the surface and near-surface structure of the energetic material rather than the material bulk. Also the probe will be transient with the EM waveform appearing as a radio frequency (RF) pulse as the probe scans the energetic material. This paper explores the electrical properties and energy localization of irregular materials excited by a temporal EM pulse. The electrical properties determined are compared with the standard mixing theories based on extreme mixing situations and using steady-state considerations alone. Time-domain monitors are also used to analyze the near-maximum temporal energy distributions for these irregular crystals.

Synthetic composites comprising irregularly-shaped crystals in a matrix are examined here with a view to characterizing their effective EM properties and so establish a baseline for remote detection and material characterization. In the past, studies of effective medium properties have used time- and frequency-domain EM simulation methods with various abstractions and simplifications made to render the simulation computationally tractable. The most common simplification is to consider regularly-shaped inclusions and sometimes a 2-D projected structure is analyzed. In the time domain, the effective permittivity has been calculated in 2-D for random mixtures using finite difference time-domain (FDTD) simulation [6] (where inclusions are disks), [7] (disks, regular polygons and fractals), and 3-D random mixtures using FDTD [8] (spheres, crosses and regular polyhedrons), and [9] (spheres and a complex yet symmetric structure). With time-domain EM analysis, regular shapes, such as cubes, spheres, and regular polygons have been studied because these enabled simplified gridding using rectangular meshing (and analytic projections onto a rectangular mesh in the case of spheres).

Frequency-domain EM analysis of 2-D random mixtures of regularly-shaped inclusions has been studied using the finite element method [10] (polygons and fractals); 3-D random mixtures of regularly-shaped inclusions using a frequency-domain finite difference method [11] (spheres), [12] (spheres, crosses, cylinders, and polyhedrons), and [13] (spheres and cylinders); and 3-D random mixtures using a frequency-domain finite element method [14] (polyhedrons), and [15], [16] (spheres). Such steady-state analyses are

limited as they, for example, do not capture temporal localization of energy.

In remote probing, a region is scanned and a steady-state is not necessarily obtained as the applied signal is effectively a radio frequency (RF) pulse. The significant internal reflections of a crystal-based composite illuminated by an RF pulse result in what is referred to as a long-tail response. This characteristic is similar to that observed with RF bandpass filters where multiple internal reflections in response to an RF pulse cannot be predicted from steady-state observations [17].

A composite of two materials will typically be anisotropic due to the fabrication or manufacturing process favoring particular crystal orientations. When the crystals are much smaller than a wavelength, in which case anisotropy results from the combination of shapes, the standard characterization procedure is to determine an effective permittivity of the mixture by averaging the extracted effective permittivities of each of three orthogonal directions [14]–[16].

Several conventional theories exist for predicting the effective permittivity of two-component mixtures with one of the components considered as an inclusion embedded in the other component. Analytic approaches, called mixing laws, to determining effective permittivity rely on a volume average of individual permittivities. While the volume fractions are important elements of mixing laws, internal sizes of the inclusions are not considered [18]. The accuracy and applicability of these laws has been questioned as they have been limited to relatively simple scenarios that are dilute and geometrically simple [18], [19]. Overall, mixing law approaches do not provide a generally acceptable solution for effective permittivity, but have been adjusted to fit experimentally derived data [18], [20]–[22].

Additional understanding of the properties of mixtures was brought about with the development of the effective medium approximation (EMA) [18], significantly discussed by Bruggeman [23] in 1935. EMA methods are applicable at low volume fractions of inclusions with the assumptions that groupings or overlapping of inclusions do not occur [18]. Since in the effective medium the energy density is seen to be uniform throughout the entire volume, EMA methods break down at higher volume fractions of inclusions since they do not take into account the interactions between the various components of a mixture [18]. So, EMA approaches do not provide an all-encompassing complete solution for two-component mixtures [18]. Results taken from computer simulations can be utilized to confirm or disprove EMA methods [18]. There are numerous methods [18] that have been studied with the aid of computers, including Fourier expansion [24], [25], FDTD [26]–[28], finite element [29]–[31], the transfer matrix method [32], and boundary-integral equations (BIE) [33]–[35]. Here, the time-domain finite integration technique (FIT) is utilized.

This paper studies two materials comprising crystals in a lossless matrix. The first is an explosive material consisting of HMX crystals [36] and the other is a material with crystals having a higher relative permittivity. For the high permittivity material, both regular and irregular shapes are studied. For both materials, realistic crystal shapes (as opposed to spheres, cubes, etc.) are considered. As such, the inclusions do not necessarily have symmetric shapes. Effective properties are extracted for the composites using forward and reverse propagation, and for various crystal orientations. The overall goals of this research are to determine under what situations irregularly shaped inclusions behave similarly to spheres (through comparison with the classical mixing rules based on spheres) and cubes in calculations of effective permittivity, and to analyze how rotation of the inclusion influences the effective permittivity of composites. Electromagnetic modeling of mixtures with irregularly shaped inclusions is computationally intensive and knowing when simpler geometries can be used is advantageous.

II. THREE-DIMENSIONAL MIXING RULES

Several conventional mixing theories exist that predict the effective properties of two-component mixtures. One of these is the Maxwell Garnett mixing theory, which provides the effective permittivity of a composite as [37]

$$\epsilon_{\text{eff}} = \epsilon_2 + 3q\epsilon_2 \frac{\epsilon_1 - \epsilon_2}{\epsilon_1 + 2\epsilon_2 - q(\epsilon_1 - \epsilon_2)}. \tag{1}$$

Here ϵ_1 is the permittivity of spherical inclusions, ϵ_2 is the permittivity of the surrounding material, and q is the volume fraction, i.e. filling factor, of the inclusions. The inclusion size here is much smaller than the EM wavelength. A few assumptions of the Maxwell Garnett mixing theory are that the inclusions are spherical in shape, the spheres do not touch each other, and the radius of an individual spherical inclusion is much smaller than the distances between the spheres [14]. That is, the mixing rule can only be properly used with composites that have a low proportion of inclusions whereas the crystals in energetic materials can have a volume fraction of up to 95%.

The second classical mixing theory is known as the Bruggeman rule [23]

$$(1-q)\frac{\epsilon_2 - \epsilon_{\text{eff}}}{\epsilon_2 + 2\epsilon_{\text{eff}}} + q\frac{\epsilon_1 - \epsilon_{\text{eff}}}{\epsilon_1 + 2\epsilon_{\text{eff}}} = 0. \tag{2}$$

As with the Maxwell Garnett mixing theory, the Bruggeman mixing rule is derived with the assumption of widely separated spherical inclusions. More complicated structures, such as irregularly-shaped crystals, are expected to provide different results [14].

As described in [38], an important assumption of the Bruggeman rule is that there is no separation between the matrix material and the inclusions. Rather, the mixture is treated as a homogenized medium over which polarizations are evaluated. Thus the Bruggeman rule treats the inclusions and surrounding material as being symmetric. The Bruggeman rule, (2), balances the components in relation to the effective medium, weighting each component by q for inclusions and $1 - q$ for the surroundings. Conversely, the Maxwell Garnett theory does not utilize such symmetry.

Mixing rules developed for composites are based on the two classical mixing rules (Maxwell Garnett and Bruggeman) but none cover all types of inclusions [14]. In this paper the applicability and limitations of the classic Maxwell Garnett and Bruggeman rules are further developed.

III. SIMULATION METHOD AND TECHNIQUE

The effective permittivity of a sample of finite thickness can be determined using measured or simulated scattering (S-) parameters as described in [39]–[42]. The time-domain finite integration technique (FIT) solver with hexahedral meshing implemented in the commercial electromagnetic (EM) package CST Microwave Studio is utilized for these simulations. This package allows complex 3D shapes to be modeled and simulated. FIT is equivalent computationally to the finite difference time-domain (FDTD) except that the time-domain Maxwell's Equations are discretized in integral form rather than differential form [42] and gridding is generalized.

The adaptive meshing algorithm used refines the mesh until convergence of electrical characterization is obtained. Refinement of the mesh by an additional step led to an effective permittivity change of less than 0.5% (indicating that acceptable accuracy had been reached). The number of mesh cells for each simulation run was at least 250,000. Computation was performed using an 80 core machine with 160 GB of RAM and clocking at 2.66 GHz. Where required, time results were Fourier transformed to yield frequency-domain characterization from an applied wideband EM pulse.

With the RF component having angular frequency ω, the free space wavenumber $k = \omega/c$ where c is the speed of light. With excitation at Port 1 (the incidence port), the wavenumber, the thickness d of the structure in the direction of propagation, and the calculated S-parameters were used to derive the refractive index n of a sample surrounded by vacuum using [41], [42]

$$n = \pm\left\{\frac{1}{kd}\arccos\left[\frac{1}{2S_{21}}(1 - S_{11}^2 + S_{21}^2)\right] + \frac{2\pi m}{kd}\right\}, \quad (3)$$

where m is an integer indicating multiple possible solutions. In (3), n is negative if the permittivity and permeability are both negative. The relative wave impedance z of the sample, with the impedance normalized to the impedance of free space, η, is [41], [42]

$$z = \pm\sqrt{\frac{(1 + S_{11})^2 - S_{21}^2}{(1 - S_{11})^2 - S_{21}^2}}. \quad (4)$$

The S-parameters in (3) and (4) are normalized to η. Information about the material can be used to remove the ambiguities in (3) and (4). When d is large compared to the wavelength λ in the medium, the branches of the arccosine function determined by m in (3) can be close together. This can make finding a unique solution for n difficult. However, in the following simulations d is less than $\lambda/4$ so that there is a unique result for n. So, the default branch of $m = 0$ and positive n is chosen in (3). A passive material means that $\Re(z)$ is positive, so that the positive branch is chosen for (4). Now, with unique solutions for n and z, the effective permittivity is [41], [42]

$$\epsilon_{\text{eff}} = \frac{n}{z}. \quad (5)$$

From [41], n can be well defined by a material that supports one propagating mode at a certain frequency, which is true here. For the frequency range studied of up to 50 GHz, there is only one propagating mode, TEM, all other modes are evanescent, and (3) and (4) use the transmission and reflection coefficients for the mode that is propagating. Thus, to make the computation tractable the bulk effective permittivity relies on an abstraction to utilize the single propagating mode rather than on evanescent modes in its derivation. The results that follow for the effective permittivities of mixtures use the procedure above to determine ϵ_{eff} unambiguously.

IV. MODELING OF IRREGULAR CRYSTALS

Several different types of irregular inclusions are analyzed here in the following subsections.

A. MODELING OF IRREGULAR CRYSTALS IN CST

An important goal of this research is modeling inclusions of a size and shape representative of materials comprising irregularly-shaped crystal inclusions. For reference, the crystal size of the irregular energetic material HMX is typically 0.15 mm [36]. This was modeled in CST as the irregularly-shaped crystal shown in Figure 1. This becomes an inclusion in a matrix modeled here as having a relative permittivity of 1. In Figure 1, the irregular crystal spans 0.15 mm in the z direction with a maximum dimension of 0.178 mm and 0.192 mm in the x and y directions respectively. The total volume of the irregular crystal is 0.00351 mm^3. The outer box shown is a cube with a side length of 0.26 mm, giving an inclusion volume fraction of $q = 0.20$ for Figure 1. For propagation in free space, a unit cell side length of 0.26 mm

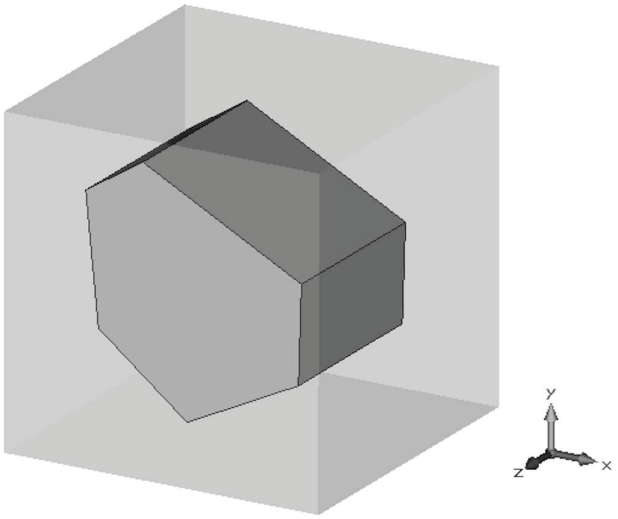

FIGURE 1. An irregularly-shaped inclusion inside an outer box. The inclusion volume fraction here is 20%. The crystal is within a cube with a side length of 0.26 mm.

corresponds to approximately 0.00087λ at the studied frequency of 1 GHz. The size of the irregular crystal is kept constant and the outer box side length is changed to obtain the various volume fractions.

EM propagation through the material is modeled using CST Microwave Studio with the crystal placed in a parallel plate transverse EM (TEM) environment [7]. With the electric field polarized in the x direction, the TEM environment is established by setting the opposite pair of normal faces in the x direction as electric walls, the opposite pair of normal faces in the y direction as magnetic walls, and the final opposite pair of normal faces in the z direction using open boundary conditions. In simulation the open faces are modeled as perfectly matched layers (PMLs) that eliminate reflections back into the TEM environment. Measurement ports are set up at the open faces (Port 1 and Port 2), defining the axis of EM propagation in the z direction, see Figure 2.

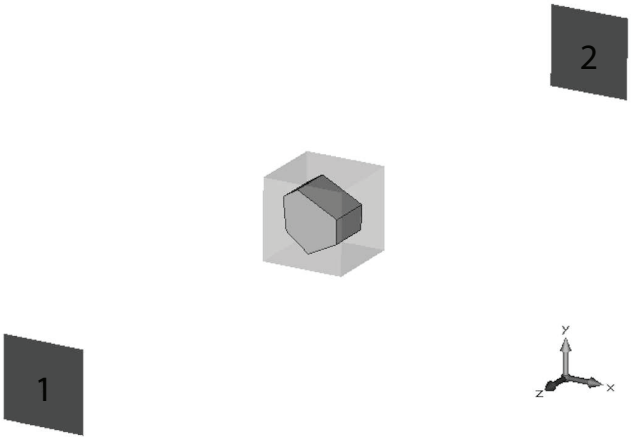

FIGURE 2. The irregular crystal of Figure 1 shown with waveguide ports (Port 1 and Port 2) set along the propagation axis, the z axis. In turn the x and y propagation directions were also considered with the crystal structure fixed in position and boundary conditions changed appropriately.

In Figure 2, the ports are separated from the mixture, providing an averaging effect similar to what happens with stand-off remote sensing. Specifically, the spacing from the waveguide ports to the structure is $\lambda/4$ of the maximum frequency component (50 GHz) of the applied RF pulse. Propagation in free space results in a separation distance of 1.5 mm for both ports in Figure 2. Measurements at the ports shown in Figure 2 were referred to reference planes on the surface of the cube also shown in Figure 2. This yielded the S-parameters used with (3) and (4) to determine the effective permittivity of the mixture calculated using a Gaussian pulse excitation signal, Fourier analyzed temporal response, and (5).

One of the issues in EM modeling is that the size of the structure that can be simulated is limited and it is necessary to establish simulation boundaries close to the structure being investigated. Thus the possible impact that the boundary conditions have on the extracted results is a concern. The TEM waveguide environment is necessary to extract the effective permittivity and the environment (i.e., the TEM set of boundary conditions) emulates a large structure that mirrors cells [16] as shown in two dimensions in Figure 3. Other periodic boundary conditions emulate structures with other arrangements of repeating cells. In the following it is shown that the boundary conditions chosen have negligible effect on energy localization and, by extrapolation, on effective permittivity.

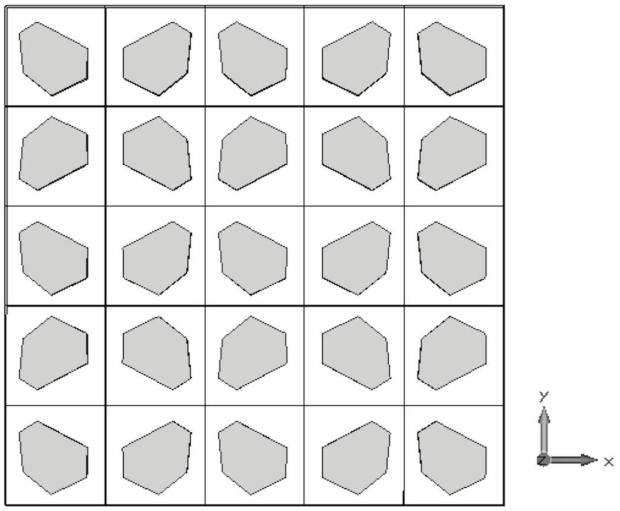

FIGURE 3. Cross section of the larger emulated structure based on a unit cell shown in Figure 1. The electric and magnetic boundary conditions of the TEM environment create electric and magnetic mirror boundaries, extended here for the 25 inner most cells.

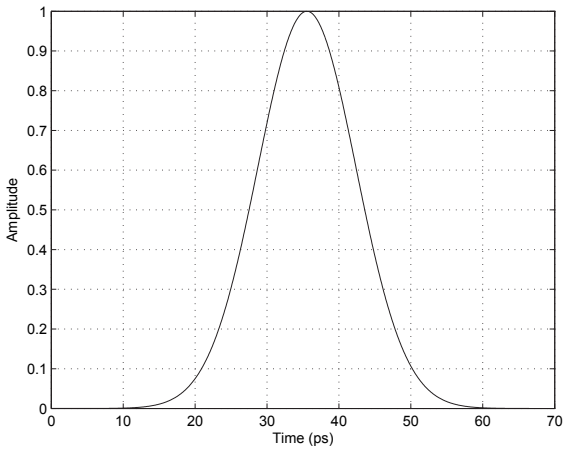

FIGURE 4. Gaussian pulse excitation signal used in simulation.

B. ENERGY LOCALIZATION

EM remote probing of compounds presents the material with an RF pulse resulting in time-localized energy concentrations rather than steady-state energy concentrations. Temporal localization of energy is explored in this section using the Gaussian pulse shown in Figure 4 (with an appreciable frequency content from 0 to 50 GHz) and the irregularly-shaped crystal shown in Figure 1. An irregularly-shaped crystal of

HMX (having low real relative permittivity of 2.03 [43], [44]) in a binder having a relative permittivity of 1, and in the TEM environment has the (near-maximum) temporal energy distribution shown in Figure 5. That is, this is the EM energy distribution close to the point in the mixture that has the highest electrical energy concentration at any position and time.

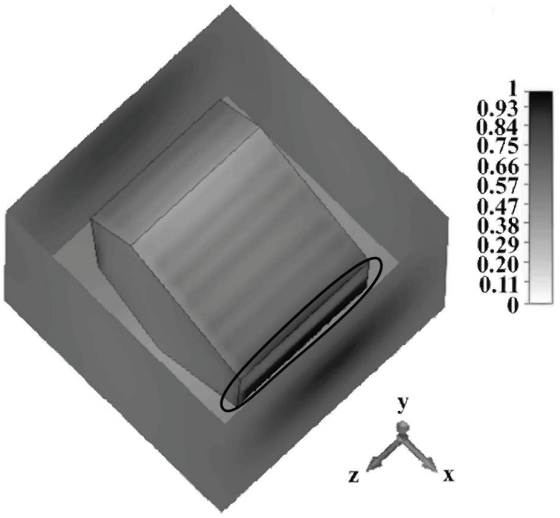

FIGURE 5. Peak electric energy density at $t = 40$ ps for the HMX-based composite (calculated as J/m^3 and here normalized to a maximum of 1) with highest density at the edges and corners indicated by the black oval. Calculated using the TEM environment with the applied electric field polarized in the x direction and propagating in the positive z direction.

It is seen that the electric energy density localizes around the edges and corners of the crystal as expected [7]. These corners and edges are specifically the ones closest to the outer box, i.e. the adjacent crystal for the emulated structure, in the polarization axis of the applied electric field (the x axis here). Before considering alternative boundary conditions, consider energy localization for a high permittivity material. For a zirconia-like high permittivity inclusion (with real relative permittivity of 28 [45]) the resulting electric energy density in the composite is given in Figure 6. The simulation conditions are the same as for Figure 5. Again the electric energy density localizes at the same corners and edges of the inclusion. Now, the peak electric energy density is approximately 8 times greater than with the composite with the HMX (low permittivity) inclusion.

To investigate the effect of the specific boundary conditions on energy localization, simulations were repeated with periodic boundary conditions at the y-z and x-z planes on the boundaries. This creates a repeating non-mirrored periodic structure in the x and y directions. With these boundary conditions it is also necessary to change the source excitation from a waveguide port to a plane wave. The plane wave is linearly polarized, propagating along the z axis with electric field polarized in the x direction. The peak electric energy densities for the low- and high-permittivity inclusions are shown in Figures 7 and 8 respectively. In Figures 7 and 8, the

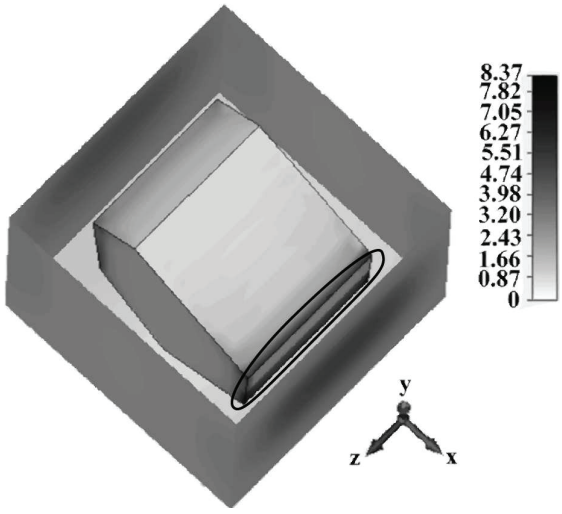

FIGURE 6. Peak electric energy density for the zirconia-like high permittivity inclusion normalized to the energy density in Figure 5. Conditions correspond to those in Figure 5.

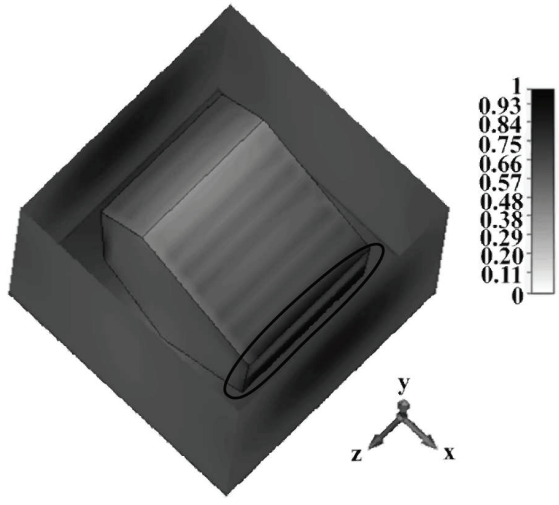

FIGURE 7. Normalized peak electric energy density for the HMX (low permittivity) inclusion with highest density at the edges and corners indicated by the black oval. Plane wave excitation and periodic boundaries are utilized. The electric field is polarized in the x direction with propagation in the positive z direction.

periodic boundary conditions result in localization of electric energy density at the corners and edges of the inclusion and the relative energy distribution is approximately identical to that obtained when the mirrored boundaries were used in simulation as in Figures 5 and 6.

Comparing the energy densities in Figures 5 and 7, and in Figures 6 and 8, and comparing the scales in Figures 6 and 8 enables the important conclusion to be reached that the simulation conditions have little effect on energy density. Figures 6 and 8 show the energy density when the high permittivity inclusion is used with the simulation reported in Figure 6 using mirror boundaries and Figure 8 using periodic boundaries. The peak energy density differs by less than 5%.

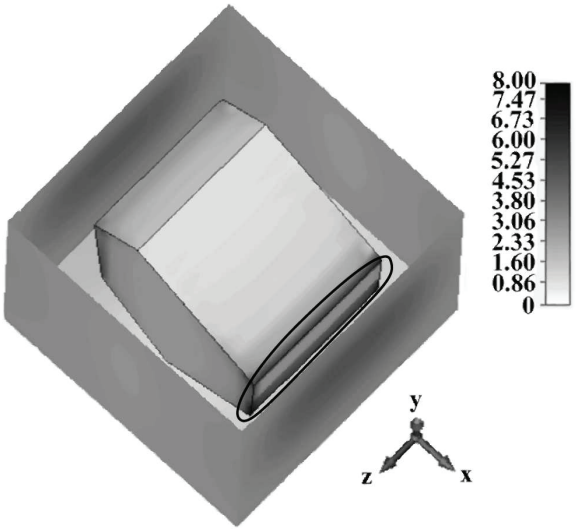

FIGURE 8. Electric energy density for the high permittivity inclusion normalized to the energy density in Figure 7 with the same simulation conditions as in Figure 7.

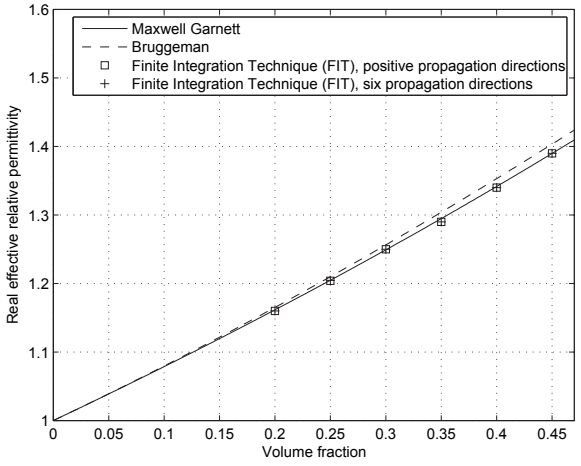

FIGURE 9. Plots of the real component of the effective relative permittivity versus volume fraction, i.e. filling factor q, for a compound with irregular HMX crystal inclusions. The squares identify the effective permittivities calculated (using EM simulated results) as the equally weighted average of the effective permittivities extracted for each of the three positive orthogonal propagation directions. The plus signs identify the effective permittivities calculated similarly but now considering both positive and negative propagation directions. Also shown are the effective permittivities calculated using the Maxwell Garnett and Bruggeman mixing theories.

Thus the results in Figures 5–8 show that there is no significant dependence of electric energy localization on simulation boundary conditions. This conclusion was reinforced by simulations with the crystal rotated and energy density again found to have little dependence on boundary conditions. With these results, the effective permittivity of the compounds can be explored without being concerned with the impact of boundary condition choice. Specifically TEM conditions are used, which enables the effective permittivity to be extracted using scattering parameters that can be conveniently extracted using the TEM environment.

C. EFFECTIVE PERMITTIVITY WITH HMX INCLUSIONS

HMX has been measured to have a relative electrical permittivity from 1 to 6 GHz of $\epsilon_r = 2.03 - \jmath 0.0035$ and this is expected to be constant up to 20 GHz [43], [44]. The flat permittivity indicates that the loss mechanism is due to dielectric relaxation and that, at least between 1 and 6 GHz, there is negligible loss due to material conductivity. The real component of the effective relative permittivity, $\Re(\epsilon_{\text{eff}})$, at 1 GHz derived from EM simulations for the HMX-based compound versus filling factor is compared to that calculated using the conventional mixing theories in Figure 9.

For the results in Figure 9 derived from EM simulations, a total of 6 propagation directions were considered in turn. Both the forward and reverse propagation directions along each of the 3 coordinate axes (x, y, and z), each corresponding to a unique polarization of electric field, E, are used to gather six independent results for effective permittivity according to (3)–(5). Figure 9 compares $\Re(\epsilon_{\text{eff}})$ taken as the arithmetic average of either just the positive propagation directions, or of all six directions. In Figure 9, the forward and reverse propagation directions for a given polarization yield the same effective permittivity within 1% and the two averaging schemes yield results within 1%. Thus, while individual permittivity values differ among x, y, and z polarizations, effective permittivity is independent of propagation direction for the same electric field polarization. As an additional test, the unit cell was doubled in the direction of propagation, and the calculated effective permittivity was found to differ from the situation of a single unit cell in the propagation direction by less than 0.05%.

At least for the low permittivity contrast material (as with the HMX compound here), the results shown in Figure 9 for the simulated effective permittivity closely follow the predictions of the Maxwell Garnett and Bruggeman mixing theories even for high filling factors. At a 45% volume fraction, $q = 0.45$, the discrepancy of the four results is less than 0.94%. The Maxwell Garnett and Bruggeman mixing theory results were based on an assumption that the inclusions are spheres and that the spheres are not close to each other (corresponding to low filling factors typically under 10%) [14]. That is, for a low permittivity contrast granular material, the Maxwell Garnett and Bruggeman mixing theories can be used with irregular inclusions and with filling factors up to 45% within 1% error.

D. EFFECTIVE PERMITTIVITY WITH HIGH PERMITTIVITY INCLUSIONS

In this section the previous results for granular materials having low permittivity inclusions are compared to those for a granular material having a high permittivity contrast between the inclusions and the matrix. The material examined has zirconia-like crystal inclusions. The zirconia-like crystals have a relative permittivity of 28, a tan δ of 0.0009 (measured

at 1 GHz [45]), have negligible conductivity, and have the same shapes as the HMX crystals to remove crystal shape as a variable. Using the same simulation environment as used previously, the calculated effective electrical permittivities at 1 GHz are compared to those derived using the Maxwell Garnett and Bruggeman mixing theories in Figure 10. As before the simulated effective permittivity is independent of propagation direction. Now, however, there is a significant difference between the effective permittivities calculated and the classic mixing theories. The discrepancy is near 1% up to a volume fraction of 0.05 growing to 22% and 61% differences from the Maxwell Garnett and Bruggeman mixing theories, respectively, at a volume fraction of 0.45. This compares to less than 1% discrepancy at this volume fraction for the lower permittivity HMX compound.

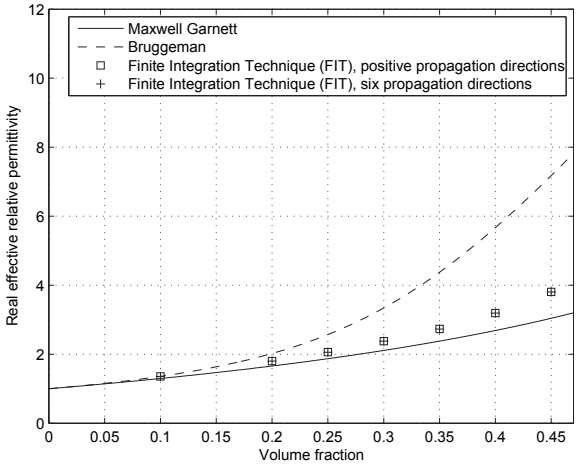

FIGURE 10. Plots of the real component of the effective relative permittivity (derived from EM simulation results) versus filling factor for an irregular high permittivity inclusion crystal. The squares indicate the equally weighted average of the effective permittivities calculated for each of the three positive orthogonal propagation directions. The plus signs indicate the equally weighted average effective permittivities of the positive and negative propagation directions (6 total). Also shown are the effective permittivities calculated using the Maxwell Garnett and Bruggeman mixing theories.

E. SUMMARY

The Maxwell Garnett and Bruggeman mixing theories are based on spherical and regularly ordered inclusions and are generally accepted as being applicable for volume fractions of 0.1. The investigations here have shown that with a small permittivity contrast between the matrix material and the inclusion (here 2.03), the Maxwell Garnett and Bruggeman mixing theories are accurate at high filling factors and for irregular structures. However, with a high permittivity contrast between the inclusion and the matrix there is a significant departure between the predictions of the conventional mixing theories and the simulated effective electrical permittivity of granular compounds. From Figure 10 it is also evident that for irregularly-shaped inclusions, high permittivity contrast between inclusion and matrix material produces significantly different results from conventional mixing theories at filling factors above 0.05. Thus for high filling factors as seen in Figure 10, the traditional mixing theories do not accurately predict the effective properties of irregularly shaped mixtures when the permittivity contrast of the inclusion and of the matrix is high. This observation is compatible with previously reported research results for high permittivity contrast when the inclusions have a regular shape [14], [16].

V. MODELING OF MULTIPLE CRYSTALS

This section continues the investigation of compounds with a high permittivity contrast scenario but now using multiple cubic crystal inclusions in an ordered arrangement in order to study the properties of a large volume with multiple inclusions but now with a regular shape. The use of a regular shape simplified the gridding used in simulation and resulted in a simulation model that fit in the available 160 GB of RAM. An example of such a structure is shown in Figure 11. In Figure 11, each cube is 0.056 mm on a side and the side length of the outer box is 1.37 mm so that the volume fraction is 5%. For propagation in free space at 1 GHz, a unit cell size of 1.37 mm corresponds to approximately 0.0046λ. Also shown in Figure 11 are Ports 1 and 2, the waveguide simulation ports. The side length of each cubic inclusion varies with volume fraction and increases to approximately 0.15 mm for a 0.95 volume fraction. The inclusions are the high permittivity material and the matrix has a relative permittivity of 1. Results of the simulated effective permittivity versus volume fraction are given at 1 GHz in Figure 12.

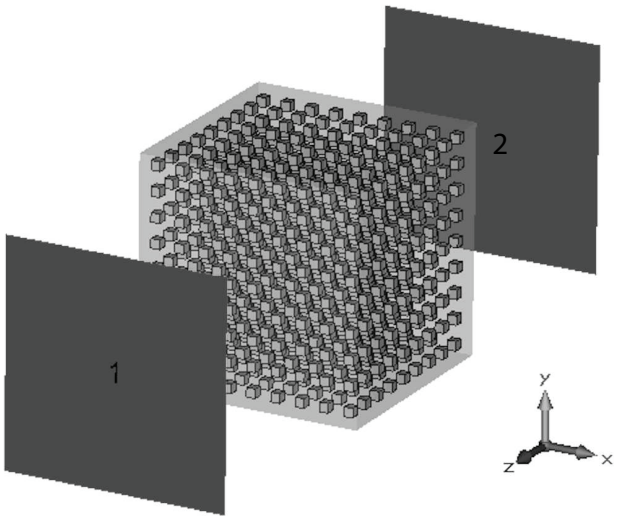

FIGURE 11. A total of 729 cubic crystals (inclusions) arranged on a grid within a free space outer block. The volume fraction of inclusions here is 5%.

In Figure 12, the effective permittivity derived from simulations closely matches the predictions of the Maxwell Garnett mixing theory for all volume fractions. Comparing Figure 12 with Figure 10, with the same high permittivity contrast, irregular inclusion shapes exhibit greater effective permittivity differences from established theory (see Figure 10) than when symmetric and

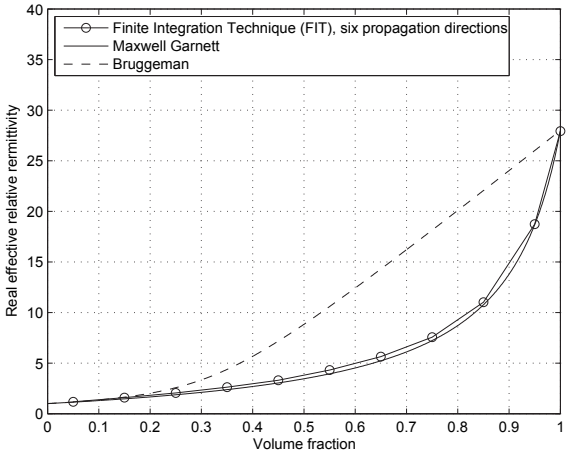

FIGURE 12. Plots of real effective relative permittivity, $\Re(\epsilon_{\text{eff}})$, versus various filling factors for high permittivity cubic inclusion crystals on a grid along with various bounds.

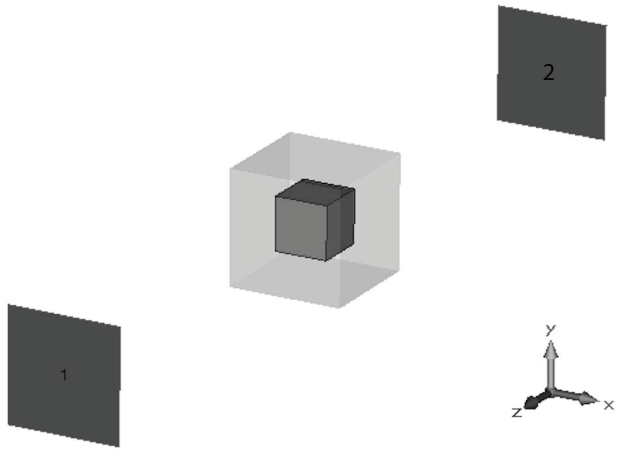

FIGURE 13. Cube-shaped high permittivity inclusion crystal at 10% volume fraction in the TEM simulation environment.

ordered inclusion crystals on a grid are considered (see Figure 12). It is also possible that the larger structure, as with the Figure 12 results, provides a greater averaging effect than the thin layer of crystals considered with Figure 10. This is examined further by considering properties of a crystal while it is rotated.

VI. ROTATED CRYSTALS

This section considers the electrical characteristics of both regularly-shaped and irregularly-shaped crystals when the crystals are rotated, with permittivity results taken at 1 GHz. Effective permittivity is calculated as the inclusion crystals are rotated, and this behavior is compared with plots of cross-sectional area. The zirconia-like crystals having high permittivity contrast are considered since these were found to have the greatest deviation from established theory previously. However, the crystal is now rotated around each of the coordinate axes (x, y, and z) to investigate the influence of crystal orientation on the determination of effective relative permittivity. These are particularly interesting effects as they form the basis of a sensing modality with the source of illumination moving rather than rotation of the crystal inclusions. Note that the manufacture of many compound objects results in aligned crystals.

A. CUBE-SHAPED ROTATED HIGH PERMITTIVITY INCLUSIONS

The analysis begins with a simple rotation scenario, a high permittivity cubic crystal inclusion with a volume fraction of 0.10, see Figure 13. In Figure 13, the inner cube has a side length of 0.195 mm and the outer box has a side length of 0.420 mm. A unit cell size of 0.420 mm corresponds to approximately 0.0014λ for propagation in free space at 1 GHz. The effect of rotation on effective permittivity with the electric field polarized in the x direction is shown in Figure 14. Figure 14 indicates that when the inclusion rotates

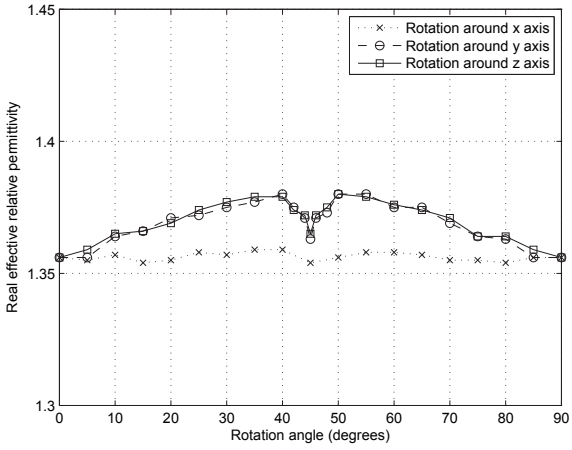

FIGURE 14. The real effective relative permittivity, $\Re(\epsilon_{\text{eff}})$, of a high permittivity cube-shaped inclusion at a filling factor of 0.10 versus rotation angle around the x, y, and z axes. Here, the electric field is polarized in the x direction.

around the x axis (the direction of electric field polarization), there is negligible change in $\Re(\epsilon_{\text{eff}})$ of the mixture. However, $\Re(\epsilon_{\text{eff}})$ does vary with rotation of the crystal around the y and z axes. Many possible sources of this rotational dependency were found with the strongest correlation being with the projection of the immediate cross-sectional area of the crystals on the plane transverse to the direction of polarization. Thus a plot of cross-sectional area fraction is shown in Figure 15. The cross-sectional area fraction with respect to a given axis is the ratio of the cross-sectional area of the inclusions projected in the plane normal to the axis to the area of the projection of the inclusions plus surrounding material in that plane. This ratio is calculated for the first crystal layer, which is the layer that interacts most strongly with an illuminating field. This ratio is shown in Figure 15 with respect to the x axis, here the electric field polarization.

By comparing Figure 14 with Figure 15, it is evident that overall the effective permittivity of the mixture with rotated

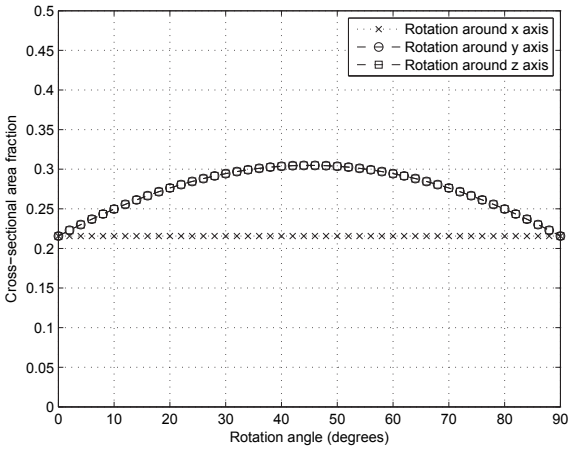

FIGURE 15. **Cross-sectional area fraction from the perspective of the *x* axis for a 10% filling factor. For other filling factors the curves are directly scaled.**

cube-shaped inclusion follows the behavior of the cross-sectional area fraction graph when rotated about the corresponding axis. If the cross-sectional area fraction is constant (as is the case for the x axis rotation here), the effective permittivity is also approximately constant. However, from 40° to 50° rotation around the y and z axes, the cross-sectional area fraction continues to increase but the effective permittivity goes down. Outside this narrow range of angles there is a high correlation of the cross-sectional area and effective permittivity.

Next, another cube-shaped high permittivity inclusion is used but this time at 20% filling factor to see how the effective permittivity versus rotation angle is altered when the filling factor is increased. The results for effective permittivity from these simulations are given in Figure 16. The same behavior seen with lower filling factor is observed but now exaggerated.

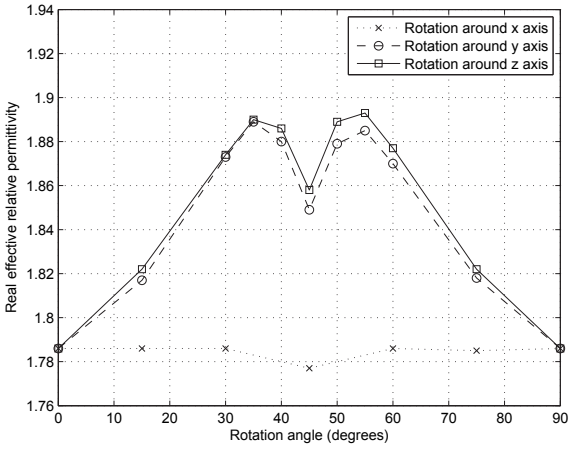

FIGURE 16. **The real effective relative permittivity, $\Re(\epsilon_{\mathbf{eff}})$, of a high permittivity cube-shaped inclusion at 20% volume fraction versus rotation angles around the *x*, *y*, and *z* axes. The electric field is polarized in the *x* direction.**

For the most part, effective permittivity follows the behavior of the cross-sectional area fraction. Now however, there is a wider region over which the cross-sectional area fraction increases but the effective permittivity goes down. In Figure 16 this dip is shown to be from 35° to 55° rotation compared to 40° to 50° rotation for the 10% volume fraction simulations in Figure 14. For both 10% and 20% volume fraction, as the crystal begins to rotate (y and z axis rotation here) the cross-sectional area fraction goes up. The volume fraction is constant but because the cross-sectional area fraction is going up more of the crystal is seen by the electric field and the effective permittivity goes up. However, an inverse relationship develops between cross-sectional area fraction and effective permittivity centered around 45°. Since the inner crystal is rotating, at 45° rotation it is closest to the nearest crystal. The crystals getting close to each other causes another phenomenon to take over where an inverse relationship develops between cross-sectional area fraction and effective permittivity.

The range over which the dips in Figures 14 and 16 occur can be understood by comparing the structures in these two situations. In the 20% volume fraction scenario in Figure 16, the inner crystal is taking up more space inside the outer box compared to the 10% volume fraction case in Figure 14. In Figure 16 the region of the dip has a larger 20° range for the 20% volume fraction scenario because (starting with 0° rotation as shown in Figure 13) it takes less rotation for the crystal to get close to the outer box. There is a smaller 10° range of the dip for the 10% volume fraction scenario in Figure 14, where because the crystal is so small within the outer box it takes close to 45° rotation for the crystals to get close enough to each other for the inverse relationship to develop.

In effect, for both the 10% and 20% volume fraction mixtures with cube-shaped inclusions all of the inclusions are rotating and at 0° and 90° the crystals are at maximum separation. At 45° the crystals are closest to each other, where fringe effects influence the effective permittivity.

B. IRREGULAR ROTATED HIGH PERMITTIVITY INCLUSIONS

In this section, the same high permittivity material properties are used for the inclusion, but this time an irregular structure is used instead of the cubes from the previous section. From Sections IV and V, the greatest deviation from established mixing theories occurred with high permittivity irregular inclusions, and these structures are studied in more detail here. The shape of the inclusion is shown in Figure 1. This allows a more realistic and complicated structure to be rotated. For all of the following rotations the volume fraction is kept constant at 20%. First, the electric field is polarized in the x direction, and results of permittivity versus rotation angle are given in Figure 17.

In Figure 17, rotation around the same axis as electric field polarization shows virtually no deviation in effective permittivity with rotation angle. However, rotation around the

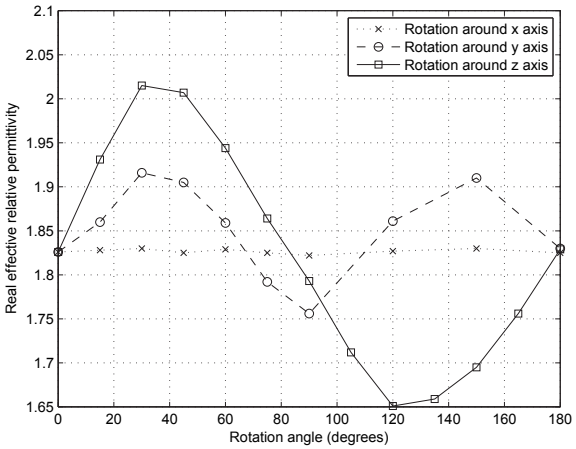

FIGURE 17. The real effective relative permittivity, $\Re(\epsilon_{\mathbf{eff}})$, of a high permittivity irregular-shaped inclusion at 20% filling factor versus rotation angle around the x, y, and z axes. The electric field is polarized in the x direction.

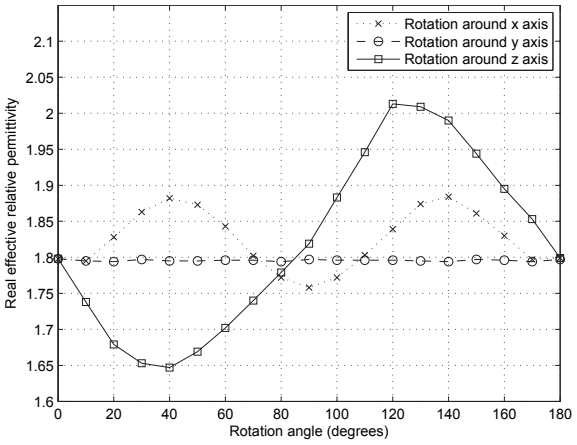

FIGURE 19. The real effective relative permittivity, $\Re(\epsilon_{\mathbf{eff}})$, of a high permittivity irregular-shaped inclusion at 20% filling factor versus rotation angle around the x, y, and z axes. The electric field is polarized in the y direction.

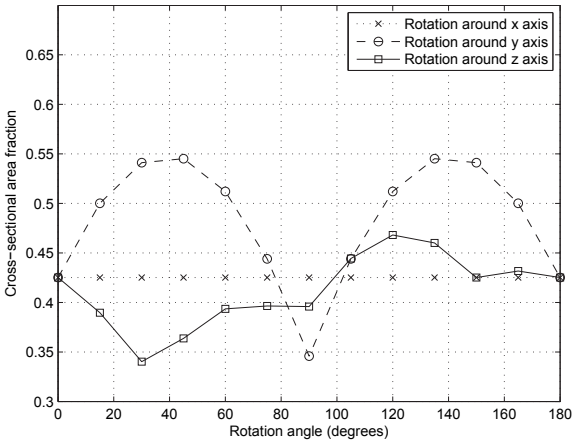

FIGURE 18. Cross-sectional area fraction of the rotated irregular crystal from the perspective of the x axis (electric field polarization axis) as the crystal is rotated around a given axis.

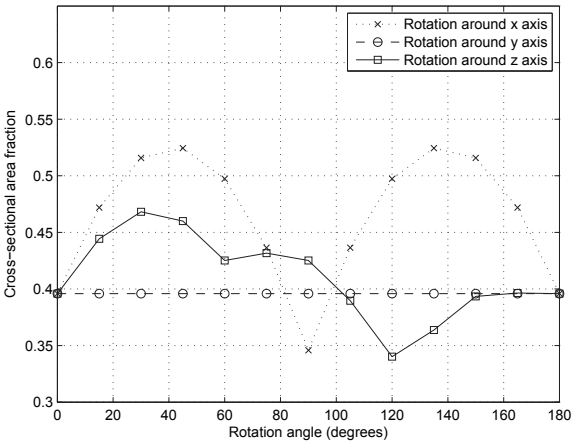

FIGURE 20. Cross-sectional area fraction of the rotated irregular crystal from the perspective of the y axis (electric field polarization axis) as the crystal is rotated around a given axis.

other axes shows unique oscillating behaviors. In an attempt to understand the reasons for these oscillations in permittivity, Figure 18 shows cross-sectional area fraction looking along the x axis (the electric field polarization axis) as the irregular crystal is rotated. By comparing Figure 17 with Figure 18, the behavior of cross-sectional area fraction with rotation follows that of effective permittivity for rotation around the x (electric field polarization axis) and y axes. The cross sectional area with rotation around the z axis oscillates just as the effective permittivity does when rotated around the z axis, but with an inverse relationship. Still, correlation between cross-sectional area fraction and effective permittivity is evident.

Next, the electric field is polarized in the y direction and the crystal is rotated around each axis. Results of effective permittivity are given in Figure 19. Again, in Figure 19 there is constant permittivity when the irregular inclusion is rotated around the y axis (electric field polarization axis), and oscillating behavior with rotation around the other axes. A plot of the cross-sectional area fraction is provided when looking from the perspective of the y axis in Figure 20. A comparison of Figure 19 with Figure 20 shows a direct correlation between cross-sectional area fraction with rotation and effective permittivity for rotation around the x and y (electric field polarization) axes. Rotation around the z axis causes cyclical variation in both figures, but with an inverse relationship.

Analyzing Figures 17–20, it is evident that there are two situations where the effective permittivity variation does not show a direct relationship to the cross-sectional area fraction. These situations are rotation about the z axis for electric field polarized in the x direction (Figures 17 and 18) and rotation about the z axis for electric field polarized in the y direction (Figures 19 and 20). Analyzing Figure 1 it is seen that these two situations involve the same type of rotation. In Figure 1, looking down the x or y axes and rotating the crystal around the z axis causes the crystal to keep the same width (in the

z direction) and rotate end over end. In this situation entire sides of the crystals are becoming close to each other. The degree of proximity is greater than in the other situations. For example, in rotation about the y axis for electric field polarized in the x direction (Figure 17), the edges rather than the faces of the crystals approach each other. So, just as in Figure 14 and Figure 16 where the cubic crystals approaching each other resulted in an inverse relationship of the effective permittivity with the cross-sectional area fraction, the situations of rotating the crystal end over end in Figures 17–20 cause enough of the crystals to be in close proximity for an inverse relationship to develop. The simulations have shown that close adjacency of neighboring inclusions results in an inverse relationship between cross-sectional area fraction and effective permittivity.

Finally, the electric field is polarized in the z direction and the crystal is rotated along each axis. The effective permittivity for this scenario is given in Figure 21. Just as shown in Figures 17 and 19, when the inclusion is rotated around the same axis as the electric field polarization in Figure 21 (z axis) there is no change in effective permittivity. Rotation around the x and y axes shows the same oscillating behavior. For comparison purposes, Figure 22 shows cross-sectional area fraction looking down the z axis (electric field polarization axis) as the irregular crystal is rotated.

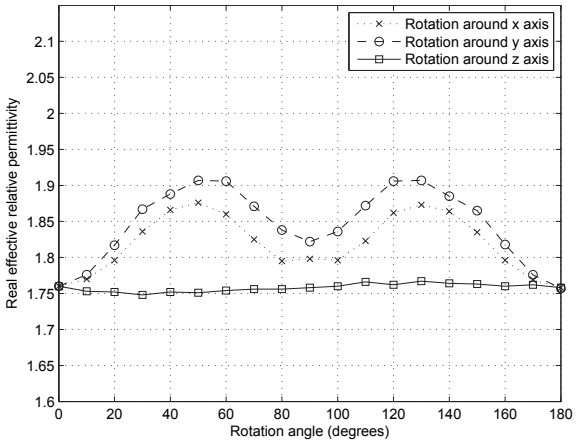

FIGURE 21. The real effective relative permittivity, $\Re(\epsilon_{eff})$, of a high permittivity irregular-shaped inclusion at 20% filling factor versus rotation angle around the x, y, and z axes. The electric field is polarized in the z direction.

Comparison between Figures 21 and 22 shows that the cross-sectional area fraction with rotation from the perspective of the z axis (electric field polarization axis) shows the same behavior as effective permittivity of the rotated inclusion for all axes. In Figures 21 and 22, there is no inverse relationship with cross-sectional area fraction because the situation of rotating end over end (z axis rotation) with sides of the crystals getting close to each other does not change the cross-sectional area fraction or the effective permittivity.

Overall, rotating the inclusion crystals provides strong evidence for a relationship between cross-sectional area

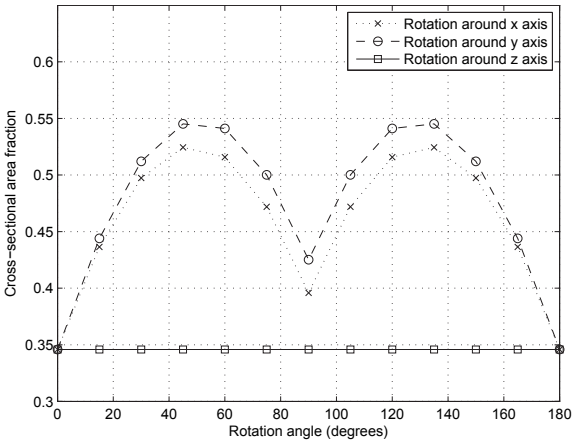

FIGURE 22. Cross-sectional area fraction of the rotated irregular crystal from the perspective of the z axis (electric field polarization axis) as the crystal is rotated around a given axis.

fraction of inclusions and effective permittivity of mixtures. For both regular and irregular crystals, the effective permittivity and cross-sectional area fraction share a direct relationship except in situations where a significant amount of the inner crystal reaches close to the outer box, or to adjacent crystals, where an inverse relationship develops.

Rotation of the inclusion crystals and changing the electric field polarization axis highlights the anisotropy of the composites studied. Effective permittivity is found to differ based on electric field polarization direction. The results in Figures 9 and 10 average together the various permittivities obtained from varying the polarization direction to obtain a single effective permittivity. The sections describing rotation also highlight anisotropy even at a constant volume fraction. We change the electric field polarization axis and rotate the inclusion crystal, and the significant differences observed are highlighted in the figures.

C. IMPACT OF OPERATING FREQUENCY

The results in the preceding sections take effective permittivity at a low frequency (1 GHz) where the inclusions are small compared to a wavelength. To see the impact on effective permittivity when the operating frequency varies, Figure 23 shows effective permittivity for the high permittivity irregular inclusion at 20% volume fraction with electric field polarized in the z direction (results from all rotations given in Figure 21) but specifically for 0° rotation. Here the unit cell has side length of 0.26 mm, corresponding to approximately 0.00087λ at 1 GHz and 0.043λ at 50 GHz for propagation in free space.

With a crystal size of approximately 0.15 mm, in Figure 23 the effective permittivity is flat through 25 GHz before starting to increase by less than 0.5% up to 50 GHz, a negligible change from the static value. Similar results were obtained for other polarizations and rotation amounts that also show a flat response across frequency.

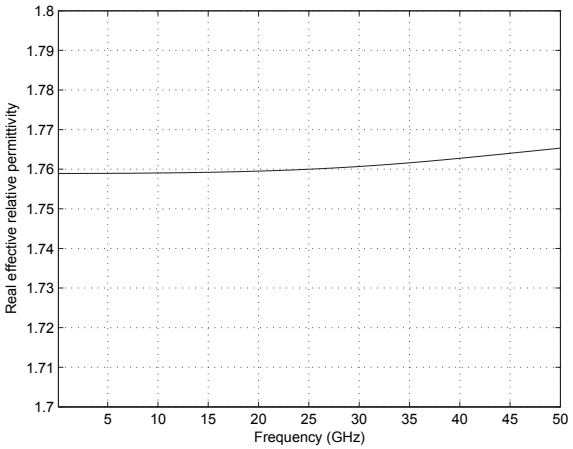

FIGURE 23. The real effective relative permittivity, $\Re(\epsilon_{\mathbf{eff}})$, of the high permittivity irregular-shaped inclusion at 20% volume fraction (results for all rotation angles given in Figure 21) for 0° rotation as a function of frequency.

VII. CONCLUSION

This paper studied the effective permittivity and electric energy localization behavior of crystal-based compounds with high and low contrast between the electrical permittivity of inclusions and the matrix. The results addressed the appropriateness of the simulation boundary conditions, applicability of traditional mixing rules, and characteristics that can lead to new sensing modalities. In particular all investigations used a temporal pulse corresponding to a remote probing scenario.

For both mirrored and periodic boundaries, electrical energy localized to the greatest extent on the edges and corners of the inclusion crystal closest to another crystal in the direction of electric field polarization. The energy localization varied with time indicating the importance of not using steady-state analysis to determine peak energy density. In particular, it is only necessary to obtain high energy concentration at one point in space and time to activate an energetic material. The energy distribution and temporal response were virtually independent of the boundary conditions used in simulation. It is therefore reasonable to assume that the boundary conditions have negligible effect on the effective permittivity of mixtures extracted from EM simulations.

The effective permittivities were extracted for both forward and reverse propagation and for each electric field polarization (x, y, and z). Since the irregular structures are not symmetric with respect to all polarization directions, it is not surprising that directional dependency of the effective permittivity was observed. However, for the same electric field polarization the effective permittivity did not depend on forward or backward propagation direction.

The classical mixing rules for spherical inclusions, Maxwell Garnett and Bruggeman, were compared to the effective permittivities extracted from EM simulations. With low permittivity contrast between inclusion and matrix material (here 2.03), there was little dependence on inclusion shape for effective permittivity up to a volume fraction of 0.45 (typically the highest volume fractions of energetic materials not of military grade). For high permittivity contrast (here 28), the effective permittivity derived was significantly different from the prediction of the classic mixing theories. For ordered cubic inclusions on a grid, the behavior of the effective permittivity derived from EM simulations was similar to that of the Maxwell Garnett theory for all volume fractions (up to 0.45), while neither Maxwell Garnett nor Bruggeman were able to correctly predict the effective permittivity of mixtures with inclusions having irregular shapes for volume fractions above 0.05.

One of the purposes of the study was to explore new sensing modalities, that is physical behaviors that could be observed remotely with the focus here being the dependence of effective permittivity on observation direction. The effect of a moving probe was emulated by rotating the crystal in the compound. When the inclusions were rotated, there was a variation in effective permittivity of the mixture leading to anisotropy even at a constant volume fraction. Thus, the effective permittivity of a mixture varies as the angle of observation changes. As the crystal inclusions were rotated (corresponding to a variation in the angle of observation for a mixture fixed in position), the effective permittivity for a given electric field polarization axis was highly correlated to the fractional cross-sectional area of the first crystal layer from the perspective of the axis of polarization. It is this first crystal layer that most strongly interacts with an applied EM pulse. An inverse relationship between effective permittivity and cross-sectional area fraction was observed. Note that manufactured energetic materials will typically have aligned crystals. That is, there is a dependency of the observed effective permittivity on the polarization and on the angle of observation. This dependency is not accounted for in the classic Maxwell Garnett and Bruggeman mixing theories and deserves further investigation.

ACKNOWLEDGMENT

The authors wish to thank D. LaBarbera for providing assistance in the methods to create randomized crystal shapes and I. Kilgore for assisting with the multi-crystal simulations.

REFERENCES

[1] F. C. De Lucia, R. S. Harmon, K. L. McNesby, R. J. Winkel, and A. W. Miziolek, "Laser-induced breakdown spectroscopy analysis of energetic materials," *Appl. Opt.*, vol. 42, no. 30, pp. 6148–6152, Oct. 2003.

[2] J. C. Carter, S. M. Angel, M. Lawrence-Snyder, J. Scaffidi, R. E. Whipple, and J. G. Reynolds, "Standoff detection of high explosive materials at 50 meters in ambient light conditions using a small Raman instrument," *Appl. Spectrosc.*, vol. 59, no. 6, pp. 769–775, 2005.

[3] D. S. Moore, "Recent advances in trace explosives detection instrumentation," *Sens. Imag., Int. J.*, vol. 8, no. 1, pp. 9–38, 2007.

[4] A. Pettersson, I. Johansson, S. Wallin, M. Nordberg, and H. Östmark, "Near real-time standoff detection of explosives in a realistic outdoor environment at 55 m distance," *Propellants Explos. Pyrotech.*, vol. 34, no. 4, pp. 297–306, Aug. 2009.

[5] A. K. Misra, S. K. Sharma, T. E. Acosta, J. N. Porter, P. G. Lucey, and D. E. Bates, "Portable standoff Raman system for fast detection of homemade explosives through glass, plastic and water," *Proc. SPIE*, vol. 8358, pp. 835811-1–835811-10, Apr. 2012.

[6] K. K. Kärkkäinen, A. H. Sihvola, and K. I. Nikoskinen, "Effective permittivity of mixtures: Numerical validation by the FDTD method," *IEEE Trans. Geosci. Remote Sens.*, vol. 38, no. 3, pp. 1303–1308, May 2000.

[7] A. Mejdoubi and C. Brosseau, "Finite-difference time-domain simulation of heterostructures with inclusion of arbitrarily complex geometry," *J. Appl. Phys.*, vol. 99, pp. 063502-1–063502-14, Mar. 2006.

[8] D. Wu, J. Chen, and C. Liu, "Numerical evaluation of effective dielectric properties of three-dimensional composite materials with arbitrary inclusions using a finite-difference time-domain method," *J. Appl. Phys.*, vol. 102, pp. 024107-1–024107-8, Jul. 2007.

[9] D. Wu, R. Qiang, J. Chen, C. Liu, M. Koledintseva, J. Drewniak, and B. Archambeault, "Numerical modeling of periodic composite media for electromagnetic shielding application," in *Proc. IEEE Int. Symp. Electromagn. Compat.*, Jul. 2007, pp. 1–5.

[10] A. Mejdoubi and C. Brosseau, "Dielectric response of perforated two-dimensional lossy heterostructures: A finite-element approach," *J. Appl. Phys.*, vol. 100, pp. 094103-1–094103-14, Nov. 2006.

[11] K. K. Kärkkäinen, A. H. Sihvola, and K. I. Nikoskinen, "Analysis of a three-dimensional dielectric mixture with finite difference method," *IEEE Trans. Geosci. Remote Sens.*, vol. 39, no. 5, pp. 1013–1018, May 2001.

[12] M. Luo, C. Liu, and H. P. Pan, "Numerical simulation on dielectric enhancement of periodic composite media using a 3D finite difference method," *Eur. Phys. J. Appl. Phys.*, vol. 52, pp. 20501-p1–20501-p8, Sep. 2010.

[13] H. Wu, D. Wu, J. Chen, and R. Liu, "Evaluation of electrical properties for complex mixtures with a low-frequency periodic technique," in *IEEE MTT-S Int. Microw. Symp. Dig.*, Jun. 2008, pp. 1349–1352.

[14] Y. Cheng, X. Chen, K. Wu, S. Wu, Y. Chen, and Y. Meng, "Modeling and simulation for effective permittivity of two-phase disordered composites," *J. Appl. Phys.*, vol. 103, pp. 034111-1–034111-8, Feb. 2008.

[15] X. Chen, Y. Cheng, K. Wu, and S. Wu, "Interfacial polarization and its influence on effective complex permittivity of mixtures," in *Proc. ISEIM*, Sep. 2008, pp. 238–241.

[16] L. Jylhä and A. H. Sihvola, "Numerical modeling of disordered mixture using pseudorandom simulations," *IEEE Trans. Geosci. Remote Sens.*, vol. 43, no. 1, pp. 59–64, Jan. 2005.

[17] G. J. Mazzaro, M. B. Steer, K. G. Gard, and A. L. Walker, "Response of RF networks to transient waveforms: Interference in frequency-hopped communications," *IEEE Trans. Microw. Theory Tech.*, vol. 56, no. 12, pp. 2808–2814, Dec. 2008.

[18] C. Brosseau, "Modelling and simulation of dielectric heterostructures: A physical survey from an historical perspective," *J. Phys. D, Appl. Phys.*, vol. 39, no. 7, pp. 1277–1294, 2006.

[19] A. Priou, *Progress in Electromagnetic Research: Dielectric Properties of Heterogeneous Materials*. New York, NY, USA: Elsevier, 1992.

[20] C. Brosseau and A. Beroual, "Computational electromagnetics and the rational design of new dielectric heterostructures," *Progr. Mater. Sci.*, vol. 48, no. 5, pp. 373–456, 2003.

[21] B. Sareni, L. Krähenbühl, A. Beroual, and C. Brosseau, "Effective dielectric constant of periodic composite materials," *J. Appl. Phys.*, vol. 80, no. 3, pp. 1688–1696, 1996.

[22] B. Sareni, L. Krähenbühl, A. Beroual, and C. Brosseau, "Effective dielectric constant of random composite materials," *J. Appl. Phys.*, vol. 81, no. 5, pp. 2375–2383, 1997.

[23] D. A. G. Bruggeman, "The calculation of various physical constants of heterogeneous substances. I. The dielectric constants and conductivities of mixtures composed of isotropic substances," *Ann. Phys.*, vol. 24, no. 132, pp. 636–679, 1935.

[24] R. Tao, Z. Chen, and P. Sheng, "First-principles Fourier approach for the calculation of the effective dielectric constant of periodic composites," *Phys. Rev. B*, vol. 41, no. 4, pp. 2417–2420, 1990.

[25] C. Zhang, B. Yang, X. Wu, T. Lu, Y. Zheng, and W. Su, "Calculation of the effective dielectric function of composites with periodic geometry," *Phys. B*, vol. 293, nos. 1–2, pp. 16–32, 2000.

[26] O. Pekonen, K. K. Kärkkäinen, A. H. Sihvola, and K. I. Nikoskinen, "Numerical testing of dielectric mixing rules by FDTD method," *J. Electromagn. Waves Appl.*, vol. 13, no. 1, pp. 67–87, 1999.

[27] A. Taflove and M. E. Brodwin, "Numerical solution of steady-state electromagnetic scattering problems using the time-dependent Maxwell's equations," *IEEE Trans. Microw. Theory Tech.*, vol. 23, no. 8, pp. 623–630, Aug. 1975.

[28] K. L. Shlager and J. B. Schneider, "A selective survey of the finite-difference time-domain literature," *IEEE Antennas Propag. Mag.*, vol. 37, no. 4, pp. 39–56, Aug. 1995.

[29] G. Mur and A. de Hoop, "A finite-element method for computing three-dimensional electromagnetic fields in inhomogeneous media," *IEEE Trans. Magn.*, vol. 21, no. 6, pp. 2188–2191, Nov. 1985.

[30] V. Myroshnychenko and C. Brosseau, "Finite-element method for calculation of the effective permittivity of random inhomogeneous media," *Phys. Rev. E*, vol. 71, no. 1, pp. 016701-1–016701-16, 2005.

[31] E. Tuncer, S. M. Gubański, and B. Nettelblad, "Dielectric relaxation in dielectric mixtures: Application of the finite element method and its comparison with dielectric mixture formulas," *J. Appl. Phys.*, vol. 89, no. 12, pp. 8092–8100, 2001.

[32] C. Barnes and J. B. Pendry, "Multiple scattering of waves in random media: A transfer matrix approach," in *Proc. R. Soc. London Ser. A, Math. Phys. Sci.*, vol. 435, no. 1893, pp. 185–196, 1991.

[33] A. Beroual, C. Brosseau, and A. Boudida, "Permittivity of lossy heterostructures: Effect of shape anisotropy," *J. Phys. D, Appl. Phys.*, vol. 33, no. 16, pp. 1969–1974, 2000.

[34] C. Brosseau, A. Beroual, and A. Boudida, "How do shape anisotropy and spatial orientation of the constituents affect the permittivity of dielectric heterostructures?" *J. Appl. Phys.*, vol. 88, no. 12, pp. 7278–7288, 2000.

[35] P. K. Ghosh and M. E. Azimi, "Numerical calculation of effective permittivity of lossless dielectric mixtures using boundary integral method," *IEEE Trans. Dielectr. Electr. Insul.*, vol. 1, no. 6, pp. 975–981, Dec. 1994.

[36] P. Chen, F. Huang, and Y. Ding, "Microstructure, deformation and failure of polymer bonded explosives," *J. Mater. Sci.*, vol. 42, no. 13, pp. 5272–5280, Jan. 2007.

[37] J. C. Maxwell Garnett, "Colours in metal glasses and in metallic films," *Phil. Trans. R. Soc. London A*, vol. 203, nos. 359–371, pp. 385–420, 1904.

[38] A. H. Sihvola, *Electromagnetic Mixing Formulas and Applications*. London, U.K.: The Institution of Electrical Engineers, 1999, ch. 9, pp. 161–163.

[39] A. M. Nicolson and G. F. Ross, "Measurement of the intrinsic properties of materials by time-domain techniques," *IEEE Trans. Instrum. Meas.*, vol. 19, no. 4, pp. 377–382, Nov. 1970.

[40] W. B. Weir, "Automatic measurement of complex dielectric constant and permeability at microwave frequencies," *Proc. IEEE*, vol. 62, no. 1, pp. 33–36, Jan. 1974.

[41] D. R. Smith, S. Schultz, P. Markoš, and C. M. Soukoulis, "Determination of effective permittivity and permeability of metamaterials from reflection and transmission coefficients," *Phys. Rev. B.*, vol. 65, no. 19, pp. 195104-1–195104-5, Apr. 2002.

[42] N. C. Dyck, R. C. Denomme, and P. M. Nieva, "Effective medium properties of arbitrary nanoparticle shapes in a localized surface plasmon resonance sensing layer," *J. Phys. Chem. C*, vol. 115, no. 31, pp. 15225–15233, Jun. 2011.

[43] B. B. Glover and W. L. Perry, "Observation of localized charge transport in isolated microscopic mats of single-wall carbon nanotubes," *J. Appl. Phys.*, vol. 101, pp. 064309-1–064309-4, Mar. 2007.

[44] W. L. Perry, J. A. Gunderson, B. B. Glover, and D. M. Dattelbaum, "Electromagnetically induced localized ignition in secondary high explosives: Experiments and numerical verification," *J. Appl. Phys.*, vol. 110, no. 3, pp. 034902-1–034902-8, 2011.

[45] M. B. Steer, *Microwave and RF Design: A Systems Approach*. Raleigh, NC, USA: SciTech, 2010, pp. 842–843.

AUSTIN J. PICKLES received the B.S. and M.S. degrees in electrical engineering from North Carolina State University (NCSU), Raleigh, NC, USA, in 2008 and 2009, respectively, and is currently pursuing the Ph.D. degree at NCSU.

He is a Graduate Research Assistant at NCSU.

MICHAEL B. STEER (S'76–M'78–SM'90–F'99) received the B.E. (Hons.) and Ph.D. degrees from the University of Queensland, Queensland, Australia, in 1976 and 1983, respectively.

He is currently the Lampe Distinguished Professor of electrical and computer engineering with North Carolina State University, Raleigh, NC, USA. He has authored or co-authored over 400 publications on topics related to microwave and millimeter-wave systems, nonlinear RF effects, circuit–electromagnetic–acoustic interactions, RF behavioral modeling, RF circuit simulation, high-speed digital design, and RF/microwave design methodology. He has co-authored *Foundations of Interconnect and Microstrip Design* (Wiley, 2000), *Multifunctional Adaptive Microwave Circuits and Systems* (SciTech, 2009), and *Microwave and RF Design: A Systems Approach* (SciTech, 2010).

Dr. Steer was a Secretary of the IEEE Microwave Theory and Techniques Society (IEEE MTT-S) in 1997 and was on the IEEE MTT-S Administrative Committee from 1998 to 2001 and 2003 to 2006. He was an Editor-in-Chief of the IEEE TRANSACTIONS ON MICROWAVE THEORY AND TECHNIQUES. He was a recipient of the Alcoa Foundation Distinguished Research Award of North Carolina State University in 2003, the Jack S. Kilby Lecturer in 2003, and the Bronze Medallion from the U.S. Army Research for Outstanding Scientific Accomplishment in 1994 and 1996. He was a recipient of the Military Medal Commander's Award for Public Service from the Commanding General of the U.S. Army Research, Development and Engineering Command in 2009. He shared the 2010 Microwave Prize of the IEEE MTT-S for the best paper on microwave engineering published in any IEEE publication in 2009. He was a recipient of the 2011 Distinguished Educator Award of the IEEE MTT-S. He was inducted into the Electronic Warfare Technology Hall of Fame sponsored by the Association of Old Crows, and was named "One of the Most Creative Teachers in the South" by Oxford American Magazine.